


X-ray astronomy comes of age

<https://doi.org/10.1038/s41586-022-04481-y>

Belinda J. Wilkes^{1,2}, Wallace Tucker¹, Norbert Schartel³ & Maria Santos-Lleo³

Received: 30 December 2019

Accepted: 28 January 2022

Published online: 8 June 2022

 Check for updates

The Chandra X-ray Observatory (Chandra) and the X-ray Multi-Mirror Mission (XMM-Newton) continue to expand the frontiers of knowledge about high-energy processes in the Universe. These groundbreaking observatories lead an X-ray astronomy revolution: revealing the physical processes and extreme conditions involved in producing cosmic X-rays in objects ranging in size from a few kilometres (comets) to millions of light years (clusters of galaxies), and particle densities ranging over 20 orders of magnitude. In probing matter under conditions far outside those accessible from Earth, they have a central role in the quest to understand our place in the Universe and the fundamental laws that govern our existence. Chandra and XMM-Newton are also part of a larger picture wherein advances in subarcsecond imaging and high-resolution spectroscopy across a wide range of wavelengths combine to provide a more complete picture of the phenomena under investigation. As these missions mature, deeper observations and larger samples further expand our knowledge, and new phenomena and collaborations with new facilities forge exciting, often unexpected discoveries. This Review provides the highlights of a wide range of studies, including auroral activity on Jupiter, cosmic-ray acceleration in supernova remnants, colliding neutron stars, missing baryons in low-density hot plasma, and supermassive black holes formed less than a billion years after the Big Bang.

Observations of cosmic X-rays, which are emitted by the hottest, densest and most violent places in the Universe, probe places and times inaccessible in other wavebands, and have fundamentally changed our understanding both of the individual types of celestial sources, and of the relationships between them¹. Even sources that are not long-term X-ray emitters become so at defining moments in their evolution, such as birth and death. The combined capabilities of the X-ray Multi-Mirror Mission (XMM-Newton) and the Chandra X-ray Observatory (Chandra) (Box 1) have facilitated multifaceted studies of all kinds of celestial sources. Although groundbreaking on their own, working in combination with current worldwide, multiwavelength capabilities, they become even more impactful, and have led a revolution in our understanding of many kinds of celestial sources.


The penetrating power of X-rays allows them to escape the clouds of gas and dust that envelope young stars, making X-ray observations critical for the detection of young stars and protostars, and tracking their early evolution. X-ray observations also provide a unique view of stellar death, particularly in massive stars that explode as a supernova and form hot, expanding remnants and extremely dense central compact objects such as neutron stars and black holes. Binary star systems are common throughout galaxies. They often interact, producing winds and jets that yield transient, X-ray emission that probes their dynamic structure and evolution. Other major galaxy components for which X-ray observations provide a critically important window are hot gas, and activity from a nuclear supermassive black hole (SMBH). The discovery of X-ray and multiwavelength emission from SMBH-powered jets has revolutionized our understanding of these powerful phenomena. X-ray surveys have provided more complete samples of active and normal galaxy populations. X-ray observations of the unexpectedly

complex structure in the hot gas in galaxy clusters, the Universe's largest gravitationally bound structures, have revealed fundamental relationships with their approximately 10^3 -times smaller, central SMBHs. Cluster X-ray emission provides constraints on cosmological parameters that complement those obtained by other methods.

Solar System

The interaction of solar energetic particles and radiation with the atmospheres of planets, their satellites and comets produces X-rays through various physical processes: scattering, fluorescence, charge exchange or the stimulation of auroral activity. Chandra and XMM-Newton have observed X-rays from Venus, Earth's magnetosphere, the Moon, Mars, Jupiter, its aurorae, some of its moons, the Io plasma torus, Saturn and its rings, Pluto, and numerous comets. These observations have implications for understanding the exoplanet response to flares from their parent stars and thus the habitability of those planets.

Observations of Jupiter have enabled detailed study of the processes involved in the large-scale energy transfer when a solar flare impacts a planetary magnetosphere and atmosphere. High-energy auroral acceleration observed in both northern and southern polar regions may be associated with the Kelvin–Helmholtz instability and/or magnetopause reconnection². The combination of Chandra and XMM-Newton X-ray data with information from the ultraviolet and particle detectors aboard the currently orbiting Juno spacecraft demonstrate that Jupiter's aurorae are produced by high-charge-state oxygen, sulfur and carbon ions³. However, rather than originating in the solar wind, these ions are precipitated into Jupiter's atmosphere from the magnetosphere.

¹Center for Astrophysics | Harvard & Smithsonian, Cambridge, MA, USA. ²School of Physics, University of Bristol, Bristol, UK. ³European Space Agency (ESA), European Space Astronomy Centre (ESAC), Villanueva de la Cañada, Spain.  e-mail: bwilkes@cfa.harvard.edu

Box 1

Chandra and XMM-Newton's X-ray revolution

In 1999, both NASA and the European Space Agency launched major observatories that advanced X-ray astronomy orders of magnitude beyond all previous capabilities and started a revolution in X-ray astronomy that continues today.

The expanded energy range of both observatories (0.3–10 keV) combine bands that previously required different instruments.

XMM-Newton is an efficient survey instrument, with 10–100 times increase in effective area compared with previous missions, a large field of view (30' diameter) and 5" spatial resolution. Chandra's low background and high spatial resolution (about 0.5"), uniquely comparable to ground-based telescopes, facilitate unconfused deep surveys to depths well matched to multiwavelength facilities, and the resolution of detailed structures in supernova remnants and clusters of galaxies. Both observatories are in a high Earth orbit and observe efficiently. Their detectors provide four-dimensional data, including the sky position, energy and time for each X-ray photon, enabling imaging, spectroscopic and timing analysis.

Both have grating spectrographs facilitating high-resolution spectroscopy of a wide range of sources. Both have (microsecond) timing resolution, and their long lifetimes uniquely facilitate tracking temporal variations of celestial sources over years to decades. They often work together, combining their complementary capabilities to understand complex targets such as clusters of galaxies.

Chandra and XMM-Newton collaborate with multiple operating X-ray satellites. Swift, launched in 2004, finds and rapidly follows-up transient targets such as γ -ray bursts and outbursting binary stars that Chandra and/or XMM-Newton track as they fade. NuSTAR, launched in 2012, the first imaging hard-X-ray telescope, partners with XMM-Newton and/or Chandra to extend spectral coverage out to 80 keV, which, for example, provides constraints on obscuration levels in AGN. The Neutron Star Interior Composition Explorer Mission (NICER), installed on the space station in 2017, constrains the very soft X-ray spectrum of transients such as neutron star X-ray binaries. The extended ROentgen Survey with an Imaging Array (eROSITA), onboard the Spectrum-X-Gamma space observatory, began a multi-epoch, 0.3–10 keV-band all-sky survey in December 2019. eROSITA detects transients and millions of new X-ray sources, providing large samples for study and follow-up observations.

Stars and exoplanets

Stars are intrinsically weak X-ray emitters, often found in crowded regions. Chandra's spatial resolution, combined with the sensitivity of both Chandra and XMM-Newton, are key to fully developing the contribution of X-ray observations to understanding star formation and evolution. X-rays penetrate obscuring material and reveal previously unseen populations. A typical Chandra observation of a single star cluster detects more than 1,000 young stars with subarcsecond position accuracy. A large fraction of these stars was not previously found because their infrared-bright disks have dissipated or been destroyed.

Much larger samples are revealing the physical conditions in stellar populations. Chandra and XMM-Newton observations of X-rays from hundreds of stellar coronae have shown a strong dependence on the rotation, magnetic activity and age of a star, facilitating distribution and dependency studies among these parameters^{4–7}.

XMM-Newton observations have also demonstrated that hot, massive stars show variability. Unusually, ζ^1 Canis Majoris shows X-ray pulsations at the same period as the star's fundamental oscillations⁸, which suggests an interaction between the oscillations and the X-ray-emitting wind in this source.

Comparative studies of many star clusters have suggested that the fraction of stars with proto-planetary disks is about 80–90% in young (1 Myr old) clusters, 20% by 5 Myr and after 10 Myr almost all disks have dissipated⁹. Evidence from the Eagle Nebula star-forming region indicates that, whereas low-mass stars have a higher disk fraction, massive stars erode and evaporate disks surrounding nearby low-mass stars¹⁰. X-ray emission from young or forming stars may also be essential for the accretion process that forms the disk as X-ray ionization is sufficient for the magneto rotational instability to induce magnetohydrodynamic turbulence¹¹.

Owing to their low luminosities and close-in habitable zones, the lowest-mass stars (M type) are the best targets for future direct (imaging) giant planet searches and indirect (transiting) discovery and characterization of potentially habitable exoplanets. On the basis of current data, giant planets seem to be rare around M dwarfs, but terrestrial planets and super-Earths (about 1.0–2.8 Earth radii) have an estimated occurrence rate about 3.5-times higher than that around solar-mass stars¹². The smaller planets may have a higher survival rate than gas giants in the intense high-energy radiation from stellar magnetic and accretion activity. For example, XMM-Newton observed an X-ray luminosity for TRAPPIST-1 comparable to the solar X-ray luminosity, although its bolometric luminosity is about 1,000-times lower¹³.

Supernovae and their remnants

Massive stars ($>10 M_{\odot}$, where M_{\odot} denotes the solar mass) shape their surroundings through mass loss in vigorous stellar winds. When these stars explode as a supernova, the fast (roughly thousands of kilometres per second) ejecta shock the circumstellar medium, producing thermal X-ray emission that can provide a window into the history and chemical composition of this mass loss, and the density of the ambient medium. The cores of these massive stars cannot be stabilized by electron-degenerate pressure, and they collapse catastrophically to form a neutron star, and then a black hole (BH) if the star is sufficiently massive¹⁴.

The rapid response time of the Neil Gehrels Swift Observatory enables fast identification of X-ray-emitting supernovae, facilitating Chandra and XMM-Newton follow-up. Implied progenitor mass-loss rates as high as about $10^{-3} M_{\odot} \text{ yr}^{-1}$ for about 10^4 yr have been detected, although typical rates are about 10–100-times less^{15–18}. As the nearest supernova observed in the past 400 years, SN 1987A provides a unique opportunity to study the first decades of a supernova's evolution and probe the circumstellar medium. The spatially resolved Chandra observations allow comparison with the features detected at optical, infrared and radio wavelengths. These data indicate that the shock wave is now leaving the dense equatorial ring of gas produced by pre-supernova winds, marking the beginning of a major change in the evolutionary phase of SN 1987A¹⁹.

Supernova remnant (SNR) shock waves probably have an important role in the acceleration of cosmic rays to petaelectronvolt energies. Energetic arguments suggest that the acceleration of particles in supernova shock waves is the source of cosmic rays (mostly protons and helium nuclei) up to the knee in the cosmic-ray spectrum at 10^{15} eV (ref. 20). The recent detection of 100-GeV γ -rays from the Tycho SNR by the Fermi Gamma-Ray Space Telescope supports this model²¹, but the γ -ray data can also be explained by energetic electrons rather than protons²². Simulations show that a cosmic-ray, current-driven instability can amplify the magnetic field and produce narrow peaks in the magnetic turbulence with a separation approximately equal to the gyroradius²³. Chandra observations of Tycho reveal a strikingly

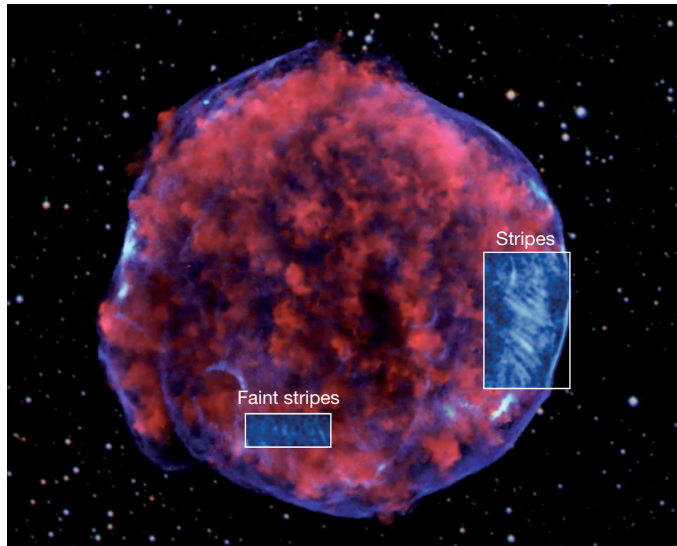


Fig. 1 | Chandra image of the Tycho supernova remnant. The inset images show close-ups of two different regions that contain the brightest stripes and fainter stripes, as labelled. The stripes are produced by synchrotron radiation from protons in regions of enhanced magnetic fields²⁴. The spacing of the stripes corresponds to the gyro-radii of protons with energies of roughly petaelectronvolts. X-ray energy: red, 1.6–2.15 keV; green, 7.15–9.3 keV; blue, 4–6 keV. Credit: X-ray, NASA/CXC/Rutgers/K. Eriksen et al.; optical, Digitized Sky Survey.

ordered pattern of non-thermal stripes (Fig. 1) with a spacing of about 0.2 pc, corresponding to the gyroradii of 10^{14} eV to 10^{15} eV protons for magnetic field strengths of about 1–10 microgauss (ref. ²⁴).

An unsolved problem is whether type Ia supernovae are produced by the merger of two white dwarfs (double-degenerate model), or when the accretion of matter from a normal solar-type star or red giant onto a white dwarf (single-degenerate model) drives it over the Chandrasekhar limit. In the former, the SN shock expands into a fairly uniform ambient medium, whereas in the latter it is non-uniform owing to the presence of the companion star and its stellar winds. These differences lead to detectable effects on the shock-wave evolution and associated X-ray light curves, images and spectra. Detailed modelling of recent X-ray data has found mixed results, favouring a double-degenerate explosion for G1.9²⁵, whereas Kepler²⁶ and RCW 86²⁷ are probably examples of single-degenerate events.

Phase-connected timing studies facilitated by the high sensitivity and timing resolution of XMM-Newton and Chandra determined the magnetic fields for four neutron stars in the centres of SNRs assuming spin-down owing to magnetic dipole radiation. All show relatively low magnetic field strengths, $B \approx 10^{10}$ – 10^{11} G (refs. ^{28–30}). However, X-ray and γ -ray observations have also revealed slowly spinning (period $P \approx 0.3$ – 10 s), highly magnetized ($B \approx 10^{14}$ G) neutron stars called magnetars³¹. XMM-Newton observations detected the first wind nebula around a magnetar³², confirming an association with supernovae and the endpoints of stellar evolution. Their slow rotation implies that magnetic energy dissipation, rather than magnetic dipole radiation, explains the steady X-ray luminosity (about 10^{32} – 10^{35} erg s⁻¹) and short, energetic flares (10^{40} – 10^{46} erg s⁻¹) that characterize magnetars. According to the magnetar model, the large internal field ultimately deforms or cracks the crust of the neutron star, disturbing the external field, causing X-ray and soft γ -ray bursts.

Beyond the accepted neutron star and magnetar classifications, continuing observations with XMM-Newton and Chandra also reveal neutron stars with unusual, magnetar-like properties. Monitoring of SGR 0418+5729 with Chandra, Swift, XMM-Newton and Rossi X-ray Timing Explorer (RXTE) shows the sporadic X-ray bursts and persistent

pulsations that are characteristic of magnetars, yet the spin-down rate implies a remarkably low $B \approx 6 \times 10^{12}$ G (ref. ³³). Phase-resolved spectroscopy in a long XMM-Newton observation detected a cyclotron absorption line that varies with rotational phase³⁴. Assuming that the absorption line is associated with protons yields $B \approx 1 \times 10^{14}$ – 2×10^{14} G, which is strong enough to break the crust and yield a magnetar-like burst. The neutron star's field may be complex, perhaps similar to a solar flare, that is a weak dipole field and a strong localized erupting loop. The pulsar (pulsing neutron star) in the SNR RCW 103 has exhibited peculiar and puzzling temporal behaviour for several decades, showing two large outbursts, one with a factor of 60 variability in 5 months. XMM-Newton higher-sensitivity observations, later confirmed by Chandra and Nuclear Spectroscopic Telescope Array (NuSTAR), revealed a 6.67-h periodicity with strong (about 50%) modulation, the longest spin period ever detected in a pulsar by orders of magnitude³⁵. In 2016, Swift detected a magnetar-like (millisecond time-scale, soft X-ray spectrum) X-ray burst. The most viable interpretation is of a magnetar that had a strong supernova fall-back accretion episode, which spun down the pulsar³⁶.

The interior structure of neutron stars remains a major open question. One suggestion is that the baryons in their cores may transition to a superfluid or superconducting state. The intermittent millisecond X-ray pulsar HETE J1900.1–2455 undergoes episodes of accretion that heat the star, followed by periods of cooling. Chandra monitoring has observed rapid atmospheric cooling to a temperature of 54 eV, implying that the core makes a negligible contribution to the total heat capacity, and providing observational support for a superfluid or superconducting scenario³⁷.

Neutron-star and black-hole binaries

Neutron stars and Galactic BHs, the endpoints of the evolution of very massive stars, provide laboratories for dense matter and curved space time, neither of which are accessible from Earth. When located near a donor star, they often become bright X-ray sources as gravitational energy is converted into electromagnetic radiation, enabling the detailed study both of the accretion physics and of the feedback and interaction with the environment.

BHs in X-ray binaries (BHXRBs) are of prime interest, because they offer the potential to measure, with fairly high accuracy, the BH mass and spin, which together fully characterize the intrinsic nature of a BH. The mass can be determined from dynamical modelling on the basis of optical data on the binary system. Two independent methods have been used to measure the spin, both assuming that the inner radius of the accretion disk lies at the innermost stable circular orbit, which depends on the BH mass and spin. In the Fe K α method, spin-dependent models of the relativistically broadened iron (Fe) line profile are compared with observations. The continuum-fitting model uses the Stefan–Boltzmann law to measure the area of the X-ray-emitting region, which depends on the mass and the spin. These methods have determined that the Cygnus X-1 BH is rotating at or near its maximum allowed spin rate^{38,39}.

Gas flows near BHs have complex dynamics, harbouring a mix of accretion onto the BH and mass loss owing to a wind. The extremely bright (about 4×10^{38} erg s⁻¹) outburst of the BHXRB V404 Cygni showed a rich, variable emission-line and continuum spectrum indicating an energetic (about 10% of the source luminosity) outflow similar to those in SMBHs (Fig. 2). The ratios of the helium (He)-like triplet lines, relative abundances of He-like and hydrogen (H)-like ions, and the line widths and luminosities constrain the parameters of the emitting gas. The Fe xxv lines are formed at a distance of about 7×10^9 cm = $5,000 R_g$ from the BH (where $R_g = GM/c^2$, the BH gravitational radius; where G is gravitational constant, M is the stellar mass and c is the speed of light). The Si XIII lines are formed farther out, at about 4×10^{11} cm (ref. ⁴⁰).

Relativistic jets are emitted by accreting BHs. The impact or feedback of jets on the environment strongly depends on their composition:

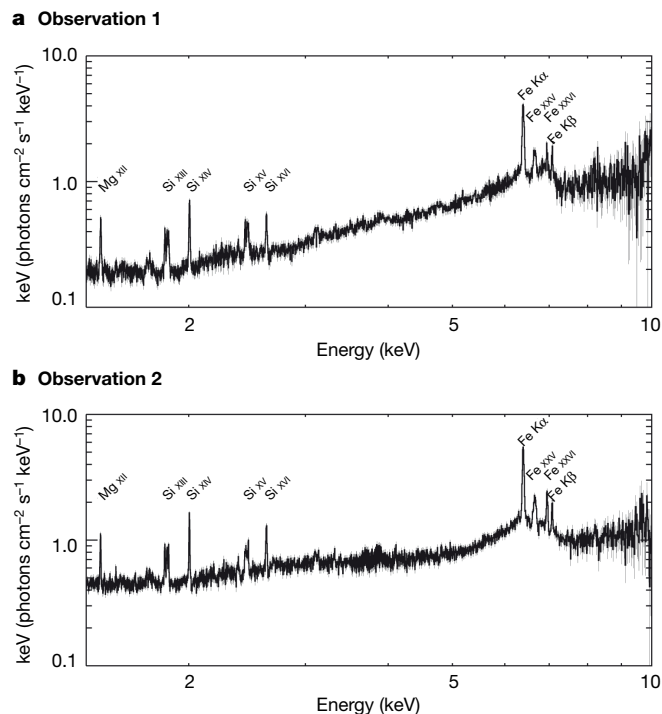


Fig. 2 | Unfolded, high-resolution Chandra HETG spectra of V404 Cygni in outburst. a, On 22 June 2015. **b**, On 23 June 2015. Emission features are observed in Mg XII, Si XIII, Si XIV, S XV, S XVI, Fe K α and Fe K β , Fe XXV and Fe XXVI. Comparison of the two spectra reveals changes in the spectral shape and a broad increase in the Fe K α line at around 6.4 keV between the two observations. Figure reproduced with permission from ref. ⁴⁰, AAS.

baryonic jets carry significantly more energy than jets composed of electrons and positrons. XMM-Newton detected X-ray emission lines from BHXR 4U 1630–47, coincident with the appearance of radio emission⁴¹. These lines arise from baryonic matter in a jet travelling at about $2/3c$. Baryonic jets are probably powered by the accretion disk and are strong sources of γ -rays and neutrino emission.

The neutron stars in X-ray binaries are remnants of supernovae. SNRs are visible for about 10^4 yr (ref. ⁴²), so the rare neutron-star X-ray binaries within SNRs probe their earliest evolutionary stages. In 2013, Chandra and radio observations discovered the SNR of the accreting neutron star Circinus X-1. An upper limit of 4,600 yr was placed on its age, making it the youngest known X-ray binary, and consistent with the system's observed rapid orbital evolution and highly eccentric orbit⁴³.

Millisecond pulsars are thought to be neutron stars that were spun-up by accretion of matter and angular momentum. Whereas the radio signal of these pulsars is powered by a rotating magnetic field, the X-ray emission is powered by accretion from a low-mass companion star. XMM-Newton and Chandra observed the transition between the radio- and X-ray-emitting states in the bursting source IGR J18245–2452⁴⁴, which was first detected by the International Gamma-Ray Astrophysics Laboratory (INTEGRAL). The large effective area of XMM-Newton enabled the detection of pulsations in the X-ray emission with a frequency consistent with that of the known pulsar. Chandra's high spatial resolution demonstrated the coincidence of the radio and X-ray positions. A few days after the month-long X-ray outburst ended, the radio signal was again detected, the most dramatic demonstration so far that the system can switch between the two states on short timescales.

Ultraluminous X-ray sources (ULXs) are spatially offset from galactic nuclei and have X-ray luminosities of about 10^{39} – 10^{41} erg s⁻¹. ULX luminosities imply that they are powered by an extreme accretion rate onto a compact stellar remnant. Although evidence is mounting

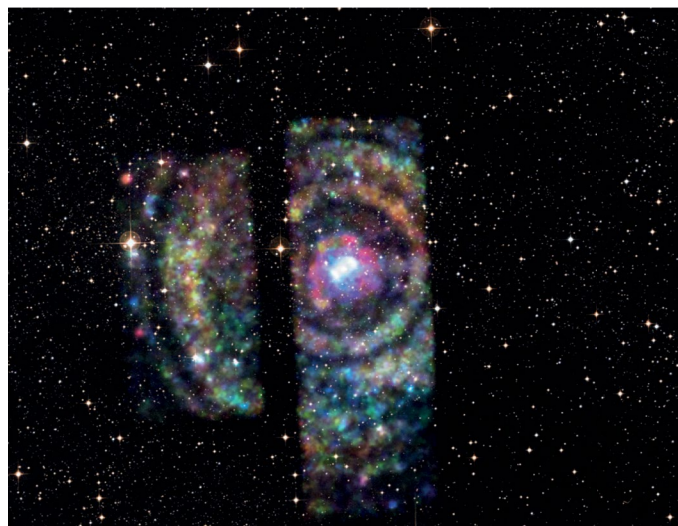


Fig. 3 | Chandra image of Circinus X-1. The image shows a set of four concentric rings around the neutron star⁴⁹. The rings are light echoes, which are produced when a burst of X-rays from Circinus X-1 scatters off clouds of dust lying between Circinus X-1 and Earth. Red, green and blue colours represent low (1–2 keV), medium (2–3 keV) and high (3–5 keV) energy X-rays, respectively. Credit: X-ray, NASA/CXC/Univ. Wisconsin-Madison/S. Heinz et al; optical, DSS.

that the majority of ULXs are neutron stars or stellar-mass BHs, the brightest few, with luminosities greater than 5×10^{40} erg s⁻¹, may be intermediate-mass BHs (IMBHs, about 10^2 – $10^5 M_{\odot}$). These may represent the missing link between stellar-mass BHs and SMBHs and could be the long-sought seeds from which SMBHs grow (see 'Galaxies, active galaxies and SMBHs').

High-resolution XMM-Newton spectra resolved atomic absorption lines, revealing fast outflowing gas in the ULXs NGC 1313 X-1 and NGC 5408 X-1⁴⁵. The outflow velocity in both sources is about $0.2c$, as predicted for stellar-mass black holes hyper-accreting above the Eddington limit (wherein the radiation pressure force on the accreting matter owing to electron scattering equals the pull of gravity). Coherent pulsations with periods of about 1 s from several bright ULXs demonstrate that some of these sources are powered by accretion onto a neutron star^{46,47}. This discovery suggests that either accretion rates are 10–500-times greater than the Eddington limit for a neutron star, or the radiation is highly beamed. Alternatively, very intense magnetic fields (about 10^{14} – 10^{15} G) could raise the Eddington limit by a factor of more than 200 by suppressing the electron-scattering cross-section⁴⁸.

Distance measurements within the Milky Way are often difficult. An ingenious method used Chandra and XMM-Newton data for neutron-star binary Circinus X-1 (Fig. 3). Four concentric X-ray light echo rings were produced when Circinus X-1 flared in late 2012 and the X-rays scattered off intervening clouds on route to Earth⁴⁹. The rings, in combination with the time delays (40 days and 80 days after the flare), determine the location of Circinus X-1 relative to the clouds, yielding a distance to Circinus X-1 of 9.4 kpc, accurate to about 10%. Conversely, this technique was used to probe the distribution and distances to interstellar dust clouds in the directions of GRB 160623A, with about 1% accuracy⁵⁰, and of V404 Cygni⁵¹, for which the distance is known to 6% accuracy from Very Long Baseline Interferometry radio observations.

The discovery of the gravitational-wave source GW170817⁵² and its electromagnetic counterpart—the result of the merger of two neutron stars—ushered in a new era of multimessenger astrophysics wherein gravitational waves and photons provide complementary views of the same source. The Laser Interferometer Gravitational-wave Observatory (LIGO)/Virgo detection implies that the merger formed an object with a mass of $2.7 M_{\odot}$. Observations at optical and infrared wavelengths

unveiled the onset and evolution of a radioactive-powered transient, known as a kilonova. Chandra observations, followed by observations at radio wavelengths, revealed a delayed, non-thermal emission component exhibiting a power-law spectrum extending from radio to X-ray frequencies^{53–55}. Continued monitoring with Chandra and XMM-Newton showed that the X-ray emission increased steadily with time, peaked at $L_x \approx 10^{40}$ erg s⁻¹ at about 160 days post-merger, and then declined with a power-law slope of about -2, indicating that our line of sight is now down the expanding cone of the decelerating relativistic jet^{56,57}. Modelling has suggested that the jet core is narrow, approximately 4°, and is viewed approximately 22° off-axis.

The discovery and detailed observations of sources similar to GRB 170817A will be necessary to reveal their nature. GRB 150101B, at redshift $z = 0.1341$, exhibited a faint, short burst characterized by a bright optical counterpart and a long-lived X-ray afterglow. Chandra's ability to distinguish the X-ray emission from GRB 150101B from that of its parent galaxy was crucial. The observed properties are consistent with an explosion viewed off-axis, optical light produced by a luminous kilonova, and X-rays that imply an extended afterglow from a jet with an opening angle of about 3–5° viewed at an angle of about 13° (ref. 58).

Galaxies, active galaxies and SMBHs

Chandra's high spatial resolution, together with the energy resolution of both Chandra and XMM-Newton, have enabled the detection, separation and study of the three major components of X-ray emission from galaxies: X-ray binaries (XRBs), which dominate the X-ray emission of normal galaxies at energies ≥ 2 keV; a hot gaseous interstellar medium (ISM) prevalent at energies $\lesssim 1$ keV; and high-energy activity produced by an SMBH in the galaxy's centre, for example, Sagittarius A* in the core of the Milky Way.

Chandra has detected and characterized previously inaccessible populations of point-like sources in all galaxies within 20–30 Mpc, finding properties consistent with a mixture of low-mass and high-mass XRBs similar to those in the Milky Way. As all the XRBs in a given galaxy are at the same distance, their absolute luminosities can be determined, and X-ray luminosity properties correlated with the star-formation rate and mass content M_* (in solar masses) of their parent stellar populations. Recently, stacking (adding together) the emission from galaxies that are individually undetected in deep surveys has confirmed the linear relationship between the XRB luminosity and M_* , an approximately linear dependence on star-formation rate and a weak dependence on redshift⁵⁹ out to redshifts of about 5.

Chandra's subarcsecond imaging and spectroscopy have firmly established the link between star formation and ISM heating via supernova explosions. In some cases (for example, M82 and NGC 253) the supernova heating rate is high enough to produce a wind of matter flowing out of the galaxy. In galaxies experiencing interactions or mergers, enhanced star formation can produce extended, luminous hot halos, a key component of galaxies. XMM-Newton's deep imaging probes their properties, including the dramatic example of the merging pair NGC 6240 found to have a large (about 100 kpc), hot (7.5 MK) X-ray halo, with a total mass of about $10^{10} M_\odot$ (ref. 60), comparable to a small galaxy group.

It is now well established that most galaxies harbour an SMBH in their centre. Accreting SMBHs, termed active galactic nuclei (AGNs), are visible as bright, nuclear sources. The most luminous, called quasars or quasi-stellar objects, outshine the stars in their host galaxies. Active accretion onto nuclear SMBHs releases large amounts of gravitational energy in the form of electromagnetic radiation and launches jets, outflows and winds. The outgoing transport of energy and momentum significantly impacts the environment, and is currently thought to be quenching star formation and interrupting the supply of accreting matter in a process called feedback.

However most nuclear SMBHs are inactive or weakly accreting. Chandra's high-spatial-resolution X-ray vision has facilitated the discovery of

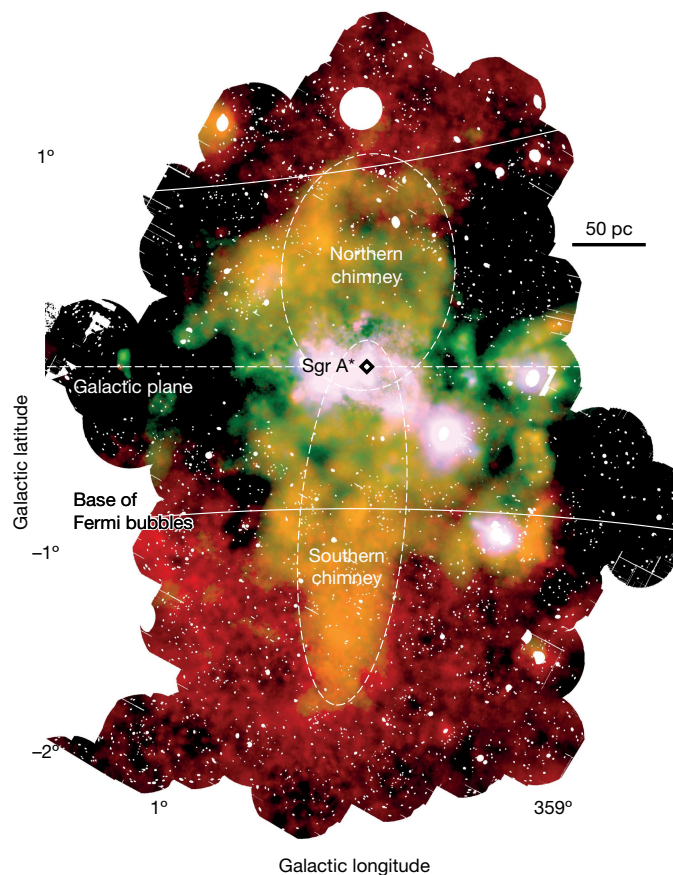


Fig. 4 | The XMM-Newton observation of the X-ray emission from the central 300 pc by 500 pc of the Milky Way. The red–green–blue image shows emission in the energy ranges: 1.5–2.6 keV; 2.35–2.56 keV, corresponding to the S xv transition; and 2.7–2.97 keV, respectively. Sagittarius A* (Sgr A*) and the central massive star cluster are located at the centre. A shell-like feature with a diameter of about 160 pc, dubbed the northern ‘chimney’, is visible to the north of Sgr A*. Diametrically opposite to the chimney with respect to Sgr A* is the bright, elongated feature dubbed the southern chimney. The north and south features have comparable brightness, extent and colour, suggesting similar emission processes (see regions enclosed by white dashed lines). Their relative placement suggests a common origin located close to Sgr A*. The white arcs correspond to the low-latitude edges of the Fermi bubbles. Figure reproduced from ref. 63, Springer Nature Ltd.

low-luminosity nuclear sources with a wide range of mass (10^6 – $10^{10} M_\odot$) in many galaxies. The resulting emission from galaxy nuclei uniquely probes the SMBH and surrounding structure.

Sagittarius A*, the SMBH in the centre of the Milky Way, is currently in a radiatively inefficient accretion phase. Deep Chandra observations allowed the tracing of an accretion flow and identified its origin with stellar winds of massive stars in the SMBH vicinity. Less than 1% of this gas accretes onto the SMBH, the remainder being ejected in a polar outflow^{61,62}. On larger scales, about one to hundreds of parsecs, XMM-Newton detected two X-ray structures, revealing exhaust channels that transport energy and mass into two big gaseous orbs called the Fermi bubbles⁶³ (Fig. 4). Sagittarius A* manifests flares of synchrotron emission confirmed by simultaneous observations of a powerful flare with XMM-Newton, NuSTAR and Spectrograph for INtegral Field Observations in the Near Infrared (SINFONI)⁶⁴. The number of bright flares seen by Chandra and XMM-Newton increased about six months after the closest approach of the gas cloud G2 to Sagittarius A*, which suggests that its passage triggered additional accretion. Gas clouds within 300 pc of Sagittarius A* emit non-thermal X-ray emission whose spatial and temporal fluctuations have been linked

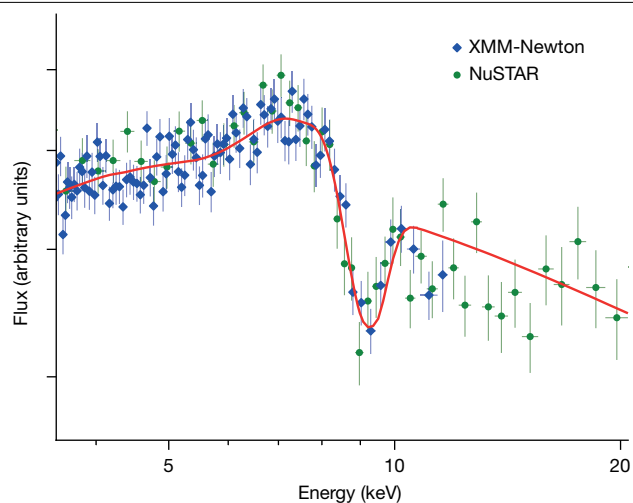


Fig. 5 | The XMM-Newton high-resolution spectrum of the luminous quasar PDS 456. A self-consistent P Cygni profile from a spherically symmetric outflow (red curve) is superposed on the XMM-Newton (in blue; ± 1 s.d. error bars) and NuSTAR (in green) data.⁷⁴ We thank Emanuele Nardini for providing this figure, adapted with permission from ref.⁷⁴, AAAS.

to past illumination by at least two bright, 10-year-long outbursts of the central SMBH⁶⁵.

Broad Fe K α emission lines in the X-ray spectra of AGNs are interpreted as fluorescence caused by reflection from the inner part of a small-scale (<1 pc) circum-nuclear torus. As for BXRBs, the line profiles, modified by relativistic effects near a rapidly rotating SMBH, can be used to measure the spin. Combined XMM-Newton and NuSTAR observations of NGC 1365 ruled out alternative models and revealed Fe K α emission from within $2.5R_g$ of an SMBH with spin, $a^* (=Jc/GM_{BH}^2$, where J is the angular momentum, and M_{BH} is the black hole mass) > 0.84 , where the maximum rate is 1 (ref.⁶⁶). The Fe emission's response to fluctuations in the incident coronal emission is delayed by light travel-time effects (reverberation), which constrains the size of the emission region. Constraints derived from measured delays in 43 XMM-Newton AGN spectra⁶⁷ have updated the relation between the amplitude of Fe lags and SMBH mass. The size of the Fe-emitting region was further constrained to less than 98 pc around the SMBH of NGC 1275, in the core of the Perseus cluster⁶⁸. Gravitational lensing has extended this technique to high-redshift quasars⁶⁹, and established X-ray microlensing events as an efficient, independent probe of nuclear structure and SMBH spin^{70–72}.

During the past decade, the inflowing and outflowing material in the vicinity of SMBHs have been studied in detail. Powerful outflows are assumed to transfer energy from an AGN to its host galaxy and any surrounding cluster, providing a feedback that regulates their evolution. Ultrafast outflows (UFO) are detected as blueshifted absorption lines with velocities of $0.03c$ to $0.3c$ in 35% of high signal-to-noise AGN spectra. Mass outflow rates of $0.01–1 M_\odot \text{ yr}^{-1}$, about 5–10% of the accretion rates, provide significant contributions to AGN cosmological feedback⁷³. The luminous quasar PDS 456 shows a roughly spherical UFO with velocity, $v_{\text{out}} = 0.35 \pm 0.02c$, and enough kinetic power to regulate SMBH and host-galaxy co-evolution⁷⁴ (Fig. 5). IRAS 13224–3809 has a $0.24c$ UFO, which responds to inner-accretion-disk fluctuations, demonstrating a connection between accretion processes occurring on very different scales⁷⁵.

Further insight into the formation and evolution of nuclear SMBHs is provided by tidal disruption events (TDE): time-constrained events owing to accretion of individual stars or gas clouds that locate nascent accretion disks and normally invisible, non-accreting SMBHs. The recent increase in optical monitoring of large sky areas has found

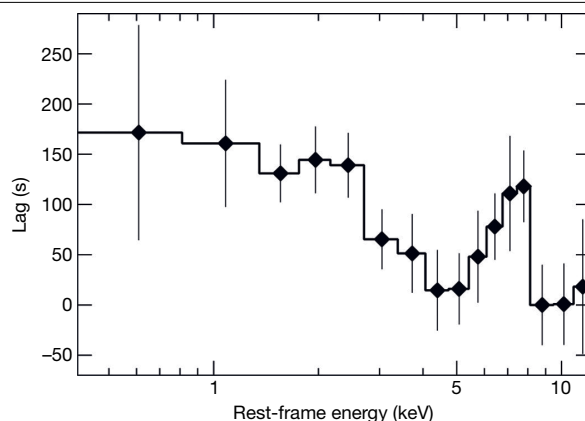


Fig. 6 | XMM-Newton time lag versus energy spectrum. The spectrum was derived from the light curve of the TDE in Swift J1644+57 in the frequency range $(2–10) \times 10^{-4}$ Hz. The zero-point has been shifted so that zero lag corresponds to the emission that varies first. The emission from about 4–5 keV and about 8–13 keV (primary continuum-dominated bands) vary first, and the Fe K α line from about 7–8 keV responds approximately 100 s later, consistent with short-timescale reverberation off an ionized accretion disk. The asymmetric profile of the Fe K α lag shows that the emission is gravitationally redshifted and therefore originates close to the central massive BH⁷⁶. The error bars are 1σ . Figure reproduced from ref.⁷⁶, Springer Nature Ltd.

more TDEs, revealing some surprising properties including: high accretion rates, IMBHs and quasi-periodic oscillations (QPOs). Reverberation mapping of gravitationally redshifted Fe K α photons from the inner accretion flow of the TDE Swift J1644+57 allowed estimates of the BH mass, suggesting an accretion rate of about 100 times the Eddington limit⁷⁶ (Fig. 6). High-resolution XMM-Newton spectra of the TDE ASASSN-14li showed winds, again suggesting a super-Eddington nascent accretion disk⁷⁷. Chandra and XMM-Newton observations of 3XMM J150052.0+015452 established the existence of a decade-long sustained TDE⁷⁸, whereas a TDE in a star cluster off-centre in its galaxy revealed evidence for an IMBH⁷⁹. X-ray QPOs, detected in only one AGN⁸⁰, were found in two TDEs: Swift J164449.3+573451 (about 200 s)⁸¹ and ASASSN-14li (131 s)⁸². Both QPOs suggest emitting regions close to the event horizon and in the latter, a rapidly spinning BH. Even more strangely, GSN 069 has shown 9-h, X-ray quasi-periodic eruptions of up to a factor of 100 since December 2018, each lasting just over an hour⁸³ (Fig. 7). A possible scenario is a second compact object orbiting the central BH, crossing the accretion disk plane and impacting the accretion disk every 9 h.

The sources detected by Chandra and XMM-Newton in the Chandra deep fields, the Cosmos field and the XMM-Newton XXL field, are predominantly AGNs and so provide an excellent database for multiple studies of their evolution up to a redshift of about five⁸⁴. Of particular interest are the SMBH co-evolution with its host galaxy⁸⁵, the effects of accretion and obscuration on AGN evolution^{86,87} and the X-ray luminosity function of AGNs^{88,89}.

XMM-Newton and Chandra observations indicate that the X-ray spectra of the highest-redshift luminous quasars ($z > 5.5$) resemble low-redshift AGNs⁹⁰, supporting a non-evolutionary scenario for the properties of luminous AGNs. Those observations imply SMBH masses ($10^9–10^{10} M_\odot$) at less than 1 Gyr after the Big Bang, requiring massive seeds ($10^5 M_\odot$) at $z \geq 10$, growing and emitting radiation by accreting leftover halo gas. Assuming standard Eddington-limited accretion, the non-detection of these seeds in the Chandra Deep Field South constrains the mass densities of MBHs, $\rho \lesssim 2.5 \times 10^2 M_\odot \text{ Mpc}^{-3}$ for $z \geq 6$ MBHs⁹¹.

The massive seeds required to explain the early appearance of luminous quasars at $z > 5.5$ motivated systematic searches for IMBH

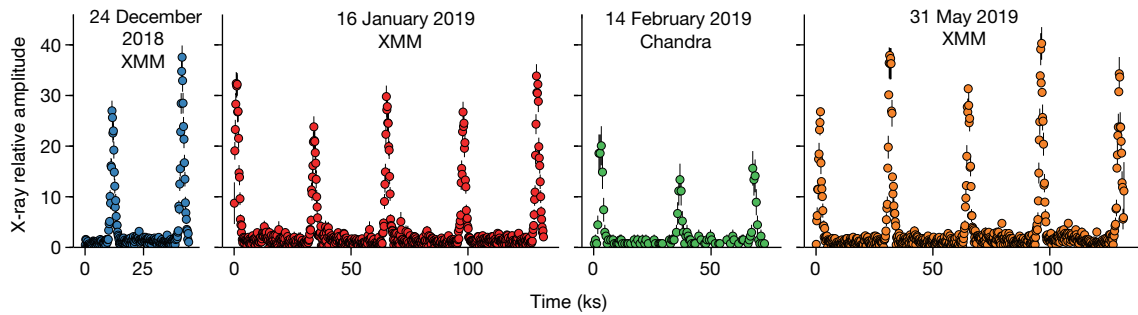


Fig. 7 | Light curves showing nine-hour quasi-periodic eruptions from the low-mass BH GSN 069 during a TDE outburst. The panels show the background-subtracted 0.4–2 keV light curve from the XMM-Newton and Chandra observations. The time axes are on the same scale highlighting the

in the local Universe with Chandra and XMM-Newton. Candidates have been identified in low-luminosity AGNs, extending the BH-bulge-mass scaling relation towards lower masses⁹², and in regular and starburst dwarf⁹³ galaxies extending down to around 50,000 M_{\odot} in the nucleus of RGG 118⁹⁴. X-ray emission from 10 out of 605 dwarf galaxies is consistent with BH masses of about 10^5 – $10^6 M_{\odot}$ (ref. ⁹⁵).

The merging of BHs is another important process for AGN and SMBH evolution over cosmic time. Chandra’s high spatial resolution is crucial for identifying mergers in nearby galaxies where both SMBHs are accreting. The binary AGN in NGC 6240 are separated by only 1 kpc (ref. ⁹⁶), whereas SDSS J1254+0846, the first detected luminous, spatially resolved binary quasar, has a separation of 21 kpc (ref. ⁹⁷). Other close binary AGN have been identified, with separations of 8 kpc, 3.4 kpc and 1.9 kpc (refs. ^{98–100}).

Galaxy clusters

X-ray observations have established that the dominant baryonic component of galaxy clusters is hot plasma, called the intracluster medium (ICM). ICM temperatures range from 10 MK to 100 MK, and its mass is about 10^{14} – $10^{15} M_{\odot}$, about 6–10 times the mass in stars. The dark-matter component of galaxy clusters has a mass about six times that of the baryonic matter and gravitationally binds the ICM to the cluster. The ICM is diffuse, with plasma number densities $n \approx 10^{-3} \text{ cm}^{-3}$, so the radiative cooling time in the outer regions is roughly billions of years, comparable to the cluster lifetime. As the ICM has been confined to galaxy clusters since they were formed, it retains a fossil-like record that includes the elements heavier than helium produced in stars and ejected into the ICM, and evidence for cosmic violence involving enormous injections of energy over roughly hundreds of millions of years from central SMBHs and high-velocity collisions between galaxies and subclusters. Evidence for such a high-velocity collision is seen in the colliding cluster pair 1E 2216.0–0401 and 1E 2215.7–0404 where Chandra and XMM-Newton observations have traced a pre-merger shock. Unusually, this shock propagates along the merger’s equatorial plane¹⁰¹, probably owing to interaction of the outer regions of the clusters.

The plasma cooling times in cluster centres is often much less than the clusters’ lifetimes¹⁰². The lack of any evidence for a sizable component of cool gas suggests that heating is occurring in the central regions, and that heating and cooling rates are linked in a negative feedback loop. This occurs naturally if an AGN–cluster feedback cycle operates wherein cooled or cooling gas fuels a central AGN that provides the power to inhibit further cooling.

Observations with Chandra and radio telescopes have provided dramatic examples of the feedback cycle in a number of AGNs located in galaxy clusters, for example, M87 in the Virgo cluster^{103,104} and NGC 1275 in the Perseus cluster¹⁰⁵. Typically, jets and lobes of high-energy particles produced by the AGNs are embedded in cavities in the hot,

similar quasi-periodic eruption recurrence time. Error bars represent 1σ confidence intervals in all panels⁸³. We thank Giovanni Miniutti for providing this figure. Figure reproduced from ref. ⁸³, Springer Nature Ltd.

X-ray-emitting gas^{102,106}. In the radio galaxy Pictor A (Fig. 8), an X-ray jet extends for over 100 kpc (320,000 light years) in projection, and is visible all the way from the core of the cluster to the terminal hotspot¹⁰⁷. In the Phoenix cluster (SPTCLJ2344–4243), at redshift $z = 0.596$, the most X-ray-luminous galaxy cluster yet discovered (L_x (2–10 keV) = $8.2 \times 10^{45} \text{ erg s}^{-1}$), Chandra data reveal the presence of deep X-ray cavities in the inner roughly 10 kpc of the hot ($kT \approx 5 \text{ keV}$, where k is the Boltzmann constant and T the temperature) gas in the cluster¹⁰⁸. A survey of 83 distant galaxy clusters suggests that the power generated by AGN feedback has remained unchanged for about 7 Gyr, over half the age of the Universe¹⁰⁹, cementing the longevity of the major paradigm change in our understanding of clusters (Box 2).

Bound by deep potential wells, galaxy clusters are self-similar and follow a well defined scaling relation between entropy and temperature. In contrast, XMM-Newton and Chandra observations show that the radio galaxies in galaxy groups produce sufficient energy to unbind a significant fraction of the hot plasma, breaking the self-similarity in these smaller systems^{110,111}.

Over the eons, galaxy clusters have been enriched with elements produced after the Big Bang, that is, all elements heavier than lithium (known as ‘metals’). As most of the baryonic matter is contained in the hot ICM, X-ray observations are key to determining the history of these elements. Extensive studies of the metal content of hundreds of clusters

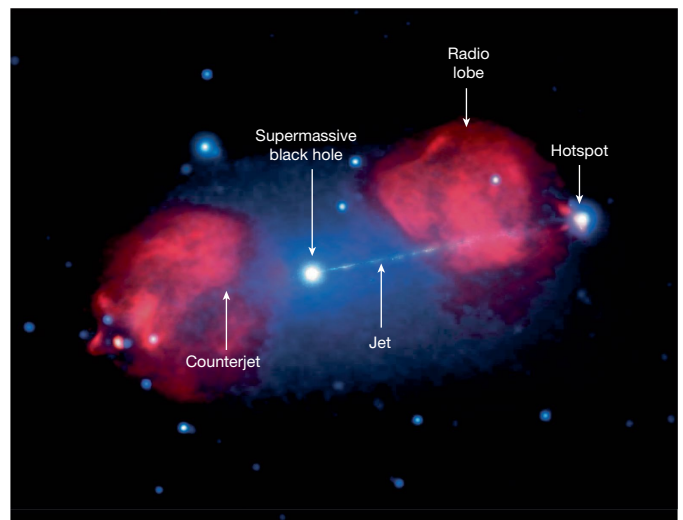


Fig. 8 | Composite image of Pictor A. The image shows the Chandra X-ray (blue) jet and the Australia Telescope Compact Array (ATCA) radio (red) lobes¹⁰⁷. The X-ray jet is 570,000 light years in length (in projection). Credit: X-ray, NASA/CXC/Univ. Hertfordshire/M. Hardcastle et al.; radio, CSIRO/ATNF/ATCA.

Box 2

Highlights of XMM-Newton and Chandra¹³⁸ paradigm changes

The first targeted Chandra observation, of a distant radio-loud active galaxy—a point source on which to focus the telescope—revealed an X-ray jet extending along the known radio jet¹³⁹, which opened up multiwavelength studies and major progress in understanding jets.

Chandra and XMM-Newton discovered long-lasting and complex structures in the hot, X-ray-bright gas of galaxy clusters. This changed the paradigm from passive cooling in cluster cores to dynamic heating and feedback from AGN outbursts, and ongoing interactions with neighbouring clusters. XMM-Newton characterizes the global properties of these large objects¹⁴⁰, whereas Chandra resolves and probes the detailed structures¹⁴¹.

Chandra's spatial resolution has been crucial in identifying ULXs, X-ray binaries with luminosities implying super-Eddington accretion. The precise locations of hundreds of ULXs have established a link with ongoing star formation in their host galaxies.

Variable X-ray spectra and light curves obtained by XMM-Newton and Chandra for a sample of magnetars demonstrated the complexity of the magnetic field compared with the previous dipole assumption^{34,142}.

Long time series of X-ray spectra obtained by XMM-Newton facilitate reverberation mapping of structures surrounding the SMBHs in AGN, revealing their mass and spin, along with the size of the X-ray emitting corona¹⁴³.

The multifaceted X-ray vision of these observatories probes through the debris of supernova explosions to find the compact remnants of the progenitor stars, detects newborn stars in the depths of gas and dust in star-forming regions, constrains velocities and physical conditions in accreting material, and much more.

using XMM-Newton and Chandra yield a consistent picture. Cluster outskirts (radii ≥ 1 Mpc) show a uniform metallicity, $Z \approx 0.2\text{--}0.3 Z_{\odot}$ (where Z_{\odot} is solar metallicity), whereas for the inner regions (radii $\lesssim 100$ kpc), $Z \approx 0.6 Z_{\odot}$ (refs. ^{112–115}). These results imply that ICM enrichment initially occurs before cluster formation. Later, the plasma in cluster centres is further enriched as the stellar populations evolve and supernovae in the central galaxies eject metals into the ISM. The metals are subsequently swept into the ICM by galactic winds, stripping by intergalactic medium ram pressure, or AGN activity¹¹³.

The discovery of CL J1001+0220, at a redshift of $z = 2.5$, extends the cluster formation epoch back by about 700 Myr to about 2.6 Gyr after the Big Bang. The presence of a hot ICM is demonstrated via the detection of extended X-ray emission in co-added images from XMM-Newton and Chandra¹¹⁶.

One of Chandra's first major discoveries in galaxy clusters was the presence of exceptionally sharp edges (less than the Coulomb mean free path) in the X-ray surface brightness where the gas density rapidly rises while the temperature falls, the opposite of shock fronts. Mergers with off-centre impacts can cause the plasma in the cluster to slosh or oscillate, creating these edges, which are similar to cold fronts in terrestrial weather patterns. The sharp edges indicate that diffusion and conduction processes are suppressed in the ICM, most likely by transverse magnetic fields^{117,118}. Chandra observations of the Centaurus cluster show one of the clearest and nearest examples of a cluster cold front¹¹⁹, a circular structure with a radius of about 30 kpc spanning nearly 180° . Large-scale cold fronts have been discovered in the outer reaches of galaxy clusters. These structures rise gradually

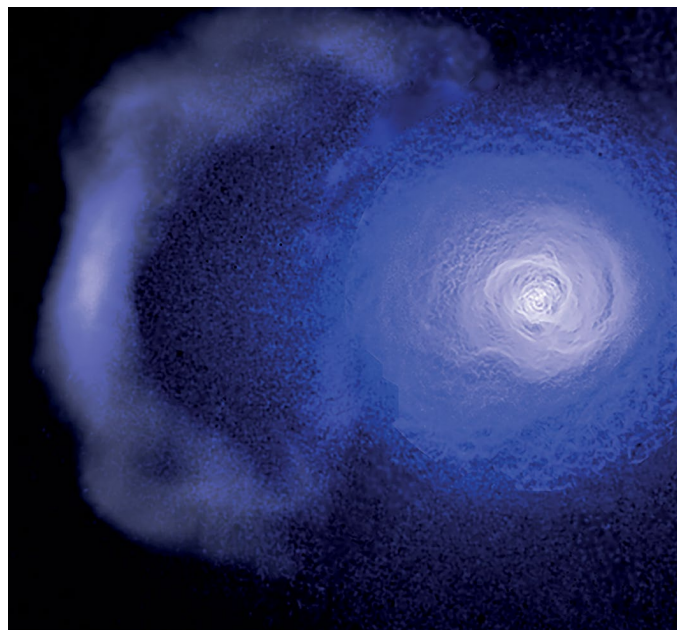


Fig. 9 | Combined Chandra, XMM-Newton and Röntgensatellit (ROSAT) images reveal a cold front in the Perseus cluster. This relatively cool (30 MK) gas has been moving outwards through hotter (80 MK) gas for about 5 Gyr (ref. ¹²⁰). The cold front spans about 2 million light years, and was probably produced when a dense gaseous cloud around a group of galaxies fell into the centre of the Perseus cluster, and then rose through the hot gas in the cluster core. The front's sharpness suggests confinement by intergalactic magnetic fields. A younger cold front can be seen in the inner part of the cluster. Credit: NASA/CXC/GSFC/S. Walker, ESA/XMM, ESA/ROSAT.

outwards with age in a characteristic spiral pattern, and embed a record of a cluster's merging activity in the ICM. In the Perseus cluster (Fig. 9), a cold front has a radius of 730 kpc, about half the cluster's virial radius¹²⁰, and an estimated age of 5 Gyr, making it the oldest coherent structure observed in the cluster. Rather than broadening through diffusion, the cold front has split into two sharp edges, consistent with abrupt jumps in density. A likely explanation is that magnetic fields can suppress diffusion for as long as several billion years.

Cosmology

XMM-Newton and Chandra X-ray observations provide complementary constraints on the inventory of dark and baryonic matter in the Universe, and the evolution of cosmological parameters.

Compared with the baryon content of the high-redshift universe (as determined from Big Bang nucleosynthesis, and also detected in the 'Lyman- α forests' absorption systems of high-redshift quasars), the local Universe contains 30–40% fewer baryons than expected by the Λ cold dark matter model (where Λ is the cosmological constant).

Cosmological hydrodynamic simulations¹²¹ predict the gradual formation of a local ($z < 1$) filamentary web of plasma in a low-density ($n = 10^{-6}\text{--}10^{-5} \text{ cm}^{-3}$), warm-hot ($T = 0.1\text{--}10 \text{ MK}$) intergalactic medium (WHIM) connecting galaxies, galaxy groups and clusters of galaxies. The WHIM is predicted to account for a sizable fraction (about 50%) of all the baryons in the local ($z < 1$) Universe, but until recently extensive observational efforts had resulted in a few marginal detections.

However, XMM-Newton has recently detected 10-MK plasma associated with large filamentary structures coherent over scales of 8 Mpc associated with the galaxy cluster Abell 2744¹²², providing direct evidence for this scenario.

Another, 1.5-Ms XMM-Newton observation enabled a 4σ detection of two absorbers of highly ionized oxygen (O VII) in the high-signal-

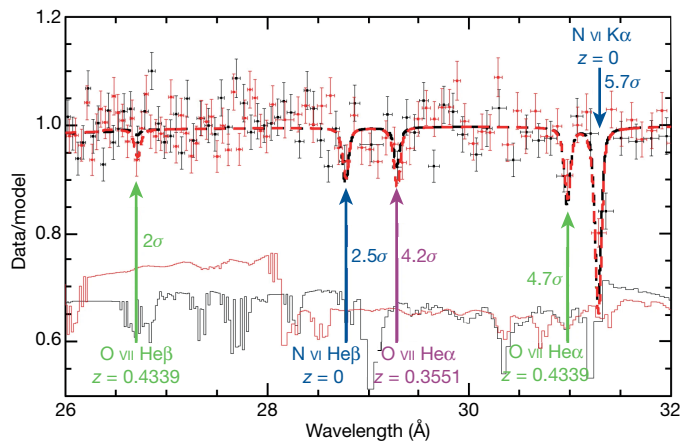


Fig. 10 | Significant absorption features (labelled) associated with the WHIM in the XMM-Newton Reflection Grating Spectrometer (RGS) spectra of the BL Lac object 1ES 1553+113. The figure shows the normalized raw RGS1 (black points; 1σ error bars) and RGS2 (red points; 1σ error bars) data (in bins with a signal-to-noise ratio per bin ≥ 30) in the wavelength interval $\lambda = 26\text{--}32 \text{ \AA}$. The thick dashed curves show the RGS1 (black) and RGS2 (red) best-fitting models, folded through the response functions of the RGSs. The thin solid curves at the bottom of the graph give the RGS1 (black) and RGS2 (red) effective areas (in arbitrary units), showing instrumental features owing to cool pixels in the dispersing detectors¹²³. Figure reproduced from ref. ¹²³, Springer Nature Ltd.

to-noise-ratio X-ray spectrum of the BL Lac object 1ES 1553+113, $z > 0.4$ (ref. ¹²³; Fig. 10) lying in regions of large galaxy overdensities. An effective 8-Ms exposure generated by stacking the Chandra/High Energy Transmission Grating (HETG) spectrum of the quasar H 1821+643, $z = 0.297$, at the redshifts of 17 known ultraviolet absorption systems also detected O VII absorption¹²⁴. Thus, detections along three different sight lines find material with observed properties consistent with WHIM simulations.

X-ray observations continue to constrain the possibilities for the identity of dark matter. A population of primordial BHs explaining the Milky Way's dark-matter content has been excluded at high significance because the predicted levels of radio and X-ray emission resulting from accretion onto these BHs has not been detected by the Very Large Array and the Chandra Source Catalog¹²⁵. Collisions between clusters of galaxies test the possibility that dark-matter particles experience non-gravitational interaction. The observation of 72 colliding clusters of galaxies with Chandra and Hubble shows that dark matter remains closely aligned with the associated stars (within $5.8 \pm 8.2 \text{ kpc}$), establishing an upper limit to the self-interaction cross-section of less than $0.47 \text{ cm}^2 \text{ g}^{-1}$ (95%)¹²⁶.

As the largest gravitationally bound structures in the Universe that form hierarchically over cosmological times¹²⁷, clusters of galaxies are an important tool for testing the fundamental assumptions of structure formation and constraining cosmological parameters. Several studies obtained cluster-based constraints on cosmological parameters, which are competitive and consistent with those from the cosmic microwave background (CMB), both Wilkinson Microwave Anisotropy Probe (WMAP) and Planck (plus WMAP polarization), type Ia supernovae and baryon acoustic oscillation data (for example, refs. ^{128,129}). However, the observed surface density of the XMM-Newton XXL (large field) survey's¹³⁰ bright cluster sample, with 100 members, is in tension with the predictions of the cosmological parameters determined from Planck data¹³¹. The XMM-Newton result is consistent with similar findings for the Sunyaev–Zeldovich clusters discovered by Planck CMB measurements¹³², and suggests either a specific rest mass of neutrinos, or time evolution of the cosmological parameters.

Quasars are the most luminous sources in the Universe and can potentially test the cosmological model at very high redshifts inaccessible with type Ia supernovae. The nonlinear correlations between luminosity and the ratio of X-ray to ultraviolet radiation^{133,134} could establish quasar as 'standard candles' and yields distances consistent with supernovae results up to $z = 1.4$. However, a significant deviation at higher redshift suggests that the dark-energy density is increasing with time.

Future

While writing this Review, both Chandra and XMM-Newton continued to demonstrate their ability to break ground (for example, the possible association of the extreme X-ray luminosity of a distant radio quasar with inverse Compton scattering of CMB photons in its relativistic jets¹³⁵) and to retain the interest of the scientific community with the continued high over-subscription of observing time.

The aging effects of both spacecraft are being managed. XMM-Newton instruments are aging as foreseen and the effects can be largely mitigated by careful and more sophisticated calibration. At some point during the 2030s, XMM-Newton's fuel will be depleted. Building on XMM-Newton's legacy, Athena, the European Space Agency's next X-ray observatory (nominal launch date is currently the end of 2032), will overlap with and then replace it. Athena¹³⁶ will have a collecting area that is about ten times that of XMM-Newton along with two instruments: a micro-calorimeter for high-spectral-resolution imaging, and a wide-field imager for observation of extended sources and surveys. Athena's main objectives are: to determine how and when large-scale hot gas structures formed and evolved; to study BH growth since the earliest epochs in the Universe; and to explore high-energy phenomena in all astrophysical contexts, some yet to be discovered.

Chandra has no life-limiting expendables and a stable orbit, and is planned to operate for many more years. Two major factors make the telescope complex to operate: heating owing to the degradation of the thermal insulation, and the continuing build-up of contaminants on the Advanced CCD Imaging Spectrometer (ACIS) detector window, which has reduced the effective area below about 1.5 keV. However, the observing efficiency of Chandra remains high (about 70%), and Chandra continues to be highly over-subscribed and to carry out cutting edge, impactful science. A Chandra successor mission, Lynx¹³⁷, was considered by the US decadal survey, Astro2020. Lynx would have roughly $0.5''$ spatial resolution, comparable to Chandra, extending to $10''$ off-axis, and an effective area of about 2 m^2 yielding approximately 50–100-times Chandra's sensitivity and 800 times the survey speed. Lynx is designed to address three main science goals: find the first SMBHs; trace the evolution of galaxies; and study the energetic lives of stars. In November 2021, Astro2020 recommended three new Great Observatories, including a high-resolution X-ray mission based on Lynx, for development in the coming decades.

1. Santos-Lleo, M., Schartel, N., Tananbaum, H., Tucker, W. & Weisskopf, M. C. The first decade of science with Chandra and XMM-Newton. *Nature* **462**, 997–1004 (2009). **Review of the first decade of Chandra and XMM science, including many of the major breakthroughs and paradigm shifts that have revolutionized X-ray astronomy and beyond.**
2. Kimura, T. et al. Jupiter's X-ray and EUV auroras monitored by Chandra, XMM-Newton, and Hisaki satellite. *J. Geophys. Res. Space Phys.* **121**, 2308–2320 (2016).
3. Dunn, W. R. et al. The independent pulsations of Jupiter's northern and southern X-ray auroras. *Nat. Astron.* **1**, 758–764 (2017).
4. Robrade, J. & Schmitt, J. H. M. M. Coronal activity cycles in action—X-rays from a Centauri A/B. Preprint at <https://arxiv.org/abs/1612.06570> (2016).
5. Robrade, J., Schmitt, J. H. M. M. & Favata, F. Coronal activity cycles in nearby G and K stars. XMM-Newton monitoring of 61 Cygni and α Centauri. *Astron. Astrophys.* **543**, 84–94 (2012).
6. Wargelin, B. J., Saar, S. H., Pojmański, G., Drake, J. J. & Kashyap, V. L. Optical, UV, and X-ray evidence for a 7-yr stellar cycle in Proxima Centauri. *Mon. Not. R. Astron. Soc.* **464**, 3281–3296 (2017).
7. Wright, N. J. & Drake, J. Solar-type dynamo behaviour in fully convective stars without a tachocline. *Nature* **535**, 526–528 (2016).
8. Oskinova, L. M. et al. Discovery of X-ray pulsations from a massive star. *Nat. Commun.* **5**, 4024 (2014).

9. Roccatagliata, V. et al. Disk evolution in OB associations: deep Spitzer/IRAC observations of IC 1795. *Astrophys. J.* **733**, 113–132 (2011).
10. Guarcello, M. G., Micela, G., Peres, G., Prisinzano, L. & Sciortino, S. Chronology of star formation and disk evolution in the Eagle Nebula. *Astron. Astrophys.* **521**, A61–A77 (2010).
11. Hirose, S. & Turner, N. J. Heating and cooling protostellar disks. *Astrophys. J.* **732L**, 30 (2011).
12. Mulders, G. et al. An increase in the mass of planetary systems around lower-mass stars. *Astrophys. J.* **814**, 130–139 (2015).
13. Wheatley, P. J., Louden, T., Bourrier, V., Ehrenreich, D. & Gillon, M. Strong XUV irradiation of the Earth-sized exoplanets orbiting the ultracool dwarf TRAPPIST-1. *Mon. Not. R. Astron. Soc.* **465**, L74–L78 (2017).
14. Janka, H.-T. Explosion mechanisms of core-collapse supernovae. *Ann. Rev. Nucl. Part. Sci.* **62**, 407–451 (2012).
15. Smith, N. et al. Endurance of SN 2005ip after a decade: X-rays, radio and H α like SN 1988Z require long-lived pre-supernova mass-loss. *Mon. Not. R. Astron. Soc.* **466**, 3021–3034 (2017).
16. Kamble, A. Progenitors of type IIb supernovae in the light of radio and X-rays from SN 2013DF. *Astrophys. J. Suppl. Ser.* **818**, 111–123 (2016).
17. Maeda, K., Katsuda, S., Bamba, A., Terada, Y. & Fukazawa, Y. Long-lasting X-ray emission from type IIb supernova 2011dh and mass-loss history of the yellow supergiant progenitor. *Astrophys. J.* **785**, 95–106 (2014).
18. Margutti, R. Results from a systematic survey of X-ray emission from hydrogen-poor superluminous SNe. *Astrophys. J.* **864**, 45–59 (2018).
19. Frank, K. A. et al. Chandra observes the end of an era for SN1987A. *Astrophys. J.* **829**, 40 (2016).
20. Blandford, R. & Eichler, D. Particle acceleration at astrophysical shocks: a theory of cosmic ray origin. *Phys. Rep.* **154**, 1–75 (1987).
21. Giordano, F. et al. Fermi Large Area Telescope detection of the young supernova remnant Tycho. *Astrophys. J.* **744**, L2–L7 (2012).
22. Atayan, A. & Dermer, C. D. Gamma rays from the Tycho supernova remnant: multi-zone versus single-zone modeling. *Astrophys. J.* **749**, L26–L30 (2012).
23. Bykov, A. M., Ellison, D. C., Osipov, S. M., Pavlov, G. G. & Uvarov, Y. A. X-ray stripes in Tycho's supernova remnant: synchrotron footprints of a nonlinear cosmic-ray-driven instability. *Astrophys. J.* **735**, L40–L50 (2011).
24. Eriksen, K. A. et al. Evidence for particle acceleration to the knee of the cosmic ray spectrum in Tycho's supernova remnant. *Astrophys. J.* **728**, L28–L32 (2011).
Chandra's exquisite spatial resolution has revealed direct evidence of cosmic-ray acceleration in an SNR that has been predicted for many years.
25. Chakraborti, S., Childs, F. & Soderberg, A. Young remnants of type Ia supernovae and their progenitors: a study of SNR G1.9+0.3. *Astrophys. J.* **819**, 37–45 (2016).
26. Burkey, M. T., Reynolds, S. P., Borkowski, K. J. & Blondin, J. M. X-ray emission from strongly asymmetric circumstellar material in the remnant of Kepler's supernova. *Astrophys. J.* **764**, 63–68 (2013).
27. Broersen, S., Chiotellis, A., Vink, J. & Bamba, A. The many sides of RCW 86: a type Ia supernova remnant evolving in its progenitor's wind bubble. *Mon. Not. R. Astron. Soc.* **441**, 3040–3054 (2014).
28. Halpern, J. P. & Gotthelf, E. V. Spin-down measurement of PSR J1852+0040 in Kesteven 79: central compact objects as anti-magnetars. *Astrophys. J.* **709**, 436–446 (2010).
29. Halpern, J. P. & Gotthelf, E. V. On the spin-down and magnetic field of the X-ray pulsar 1E 1207.4–5209. *Astrophys. J.* **733**, L28 (2011).
30. Gotthelf, J. E. V., Halpern, J. P. & Alford, J. The spin-down of PSR J0821–4300 and PSR J1210–5226: confirmation of central compact objects as anti-magnetars. *Astrophys. J.* **765**, 58–73 (2013).
31. Mereghetti, S. The strongest cosmic magnets: soft gamma-ray repeaters and anomalous X-ray pulsars. *Astron. Astrophys. Rev.* **15**, 225–287 (2008).
32. Younes, G. et al. The wind nebula around magnetar Swift J1834.9–0846. *Astrophys. J.* **824**, 138–149 (2016).
33. Rea, N. et al. The outburst decay of the low magnetic field magnetar SGR 0418+5729. *Astrophys. J.* **770**, 65–78 (2013).
34. Tiengo, A. et al. A variable absorption feature in the X-ray spectrum of a magnetar. *Nature* **500**, 312–314 (2013).
35. De Luca, A., Caraveo, P. A., Mereghetti, S., Tiengo, A. & Bignami, G. F. A long-period, violently variable X-ray source in a young supernova remnant. *Science* **313**, 81–817 (2006).
36. Rea, N. et al. Magnetar-like activity from the central compact object in the SNR RCW103. *Astrophys. J.* **828**, L13–L18 (2016).
37. Degenaar, N., Ootes, L. S., Reynolds, M. T., Wijnands, R. & Page, D. A cold neutron star in the transient low-mass X-ray binary HETE J1900.1–2455 after 10 yr of active accretion. *Mon. Not. R. Astron. Soc.* **465**, L10–L14 (2017).
38. Gou, L. et al. Confirmation via the continuum-fitting method that the spin of the black hole in Cygnus X-1 is extreme. *Astrophys. J.* **790**, 29–41 (2014).
39. Duro, R. et al. The broad iron K α line of Cygnus X-1 as seen by XMM-Newton in the EPIC-pn modified timing mode. *Astron. Astrophys.* **533**, L3–L6 (2011).
40. King, A. L., Miller, J. M., Raymond, J., Reynolds, M. T. & Morningstar, W. High-resolution Chandra HETG spectroscopy of V404 Cygni in outburst. *Astrophys. J.* **813**, L37–L34 (2015).
41. Diaz Trigo, M., Miller-Jones, J. C. A., Migliari, S., Broderick, J. W. & Tzioumis, T. Baryons in the relativistic jets of the stellar-mass black-hole candidate 4U1630–47. *Nature* **504**, 260–262 (2013).
42. Vink, J. Supernova remnants: the X-ray perspective. *Astron. Astrophys. Rev.* **20**, 49–168 (2012).
43. Heinz, S. et al. The youngest known X-ray binary: Circinus X-1 and its natal supernova remnant. *Astrophys. J.* **779**, 171–178 (2013).
Uses the X-ray light echoes from dust clouds along the line of sight during a Circinus X-1 outburst to accurately measure its distance and thus luminosity and age.
44. Papitto, A. et al. Swings between rotation and accretion power in a binary millisecond pulsar. *Nature* **501**, 517–520 (2013).
45. Pinto, C., Middleton, M. J. & Fabian, A. C. Resolved atomic lines reveal outflows in two ultraluminous X-ray sources. *Nature* **533**, 64–67 (2016).
46. Carpano, S., Haberl, F., Maitra, C. & Vasilopoulos, G. Discovery of pulsations from NGC 300 ULX1 and its fast period evolution. *Mon. Not. R. Astron. Soc.* **476**, L45–L49 (2018).
47. Walton, D. J. et al. Evidence for pulsar-like emission components in the broadband ULX sample. *Astrophys. J.* **856**, 128–140 (2018).
48. Brightman, M. et al. Magnetic field strength of a neutron-star-powered ultraluminous X-ray source. *Nat. Astron.* **2**, 312–313 (2018).
49. Heinz, S. et al. Lord of the rings: a kinematic distance to Circinus X-1 from a giant X-ray light echo. *Astrophys. J.* **806**, 265–283 (2015).
50. Pintore, F. et al. Behind the dust curtain: the spectacular case of GRB 160623A. *Mon. Not. R. Astron. Soc.* **472**, 1465–1472 (2017).
51. Heinz, S. et al. A joint Chandra and Swift view of the 2015 X-ray dust-scattering echo of V404 Cygni. *Astrophys. J.* **825**, 15–34 (2016).
52. Abbott, B. P. et al. Multi-messenger observations of a binary neutron star merger. *Astrophys. J.* **848**, L12–L70 (2017).
53. Haggard, D. et al. A deep Chandra X-ray study of neutron star coalescence GW170817. *Astrophys. J.* **848**, L25–L30 (2017).
54. Margutti, R. et al. The electromagnetic counterpart of the binary neutron star merger LIGO/Virgo GW170817. V. Rising X-ray emission from an off-axis jet. *Astrophys. J.* **848**, L20–L26 (2017).
55. Troja, E. et al. The X-ray counterpart to the gravitational-wave event GW170817. *Nature* **551**, 71–74 (2017).
These three papers (refs. 53, 54 and 55) report the X-ray detections of the gravitational-wave source GW170817, the first electromagnetically detected gravitational-wave source, and a neutron star–neutron star merger.
56. Troja, E. et al. A year in the life of GW 170817: the rise and fall of a structured jet from a binary neutron star merger. *Mon. Not. R. Astron. Soc.* **489**, 1919–1926 (2019).
57. D'Avanzo, P. et al. The evolution of the X-ray afterglow emission of GW170817/GRB170817A in XMM-Newton observations. *Astron. Astrophys.* **613**, L1–L5 (2018).
58. Troja, E. et al. A luminous blue kilonova and an off-axis jet from a compact binary merger at $z = 0.1341$. *Nat. Commun.* **9**, 4089 (2018).
59. Fornasini, F. M. et al. Low-luminosity AGN and X-ray binary populations in COSMOS star-forming galaxies. *Astrophys. J.* **865**, 43–60 (2018).
60. Nardini, E. et al. The exceptional soft X-ray halo of the galaxy merger NGC 6240. *Astrophys. J.* **765**, 141–160 (2013).
61. Roberts, S. R., Jiang, Y.-F., Wang, Q. D. & Ostriker, J. P. Towards self-consistent modelling of the Sgr A* accretion flow: linking theory and observation. *Mon. Not. R. Astron. Soc.* **466**, 1477–1490 (2017).
62. Wang, Q. D. et al. Dissecting X-ray-emitting gas around the center of our Galaxy. *Science* **341**, 981–983 (2013).
63. Ponti, G. et al. An X-ray chimney extending hundreds of parsecs above and below the Galactic Centre. *Nature* **567**, 347–350 (2019).
XMM-Newton has mapped X-ray emission extending up to and into the 'Fermi bubble' region.
64. Ponti, G. et al. A powerful flare from Sgr A* confirms the synchrotron nature of the X-ray emission. *Mon. Not. R. Astron. Soc.* **468**, 2447–2468 (2017).
65. Terrier, R. et al. An X-ray survey of the central molecular zone: variability of the Fe K α emission line. *Astron. Astrophys.* **612**, A102–A117 (2018).
66. Risaliti, G. et al. A rapidly spinning supermassive black hole at the centre of NGC 1365. *Nature* **494**, 449–451 (2013).
67. Kara, E. et al. A global look at X-ray time lags in Seyfert galaxies. *Mon. Not. R. Astron. Soc.* **462**, 511–531 (2016).
68. Miller, J. M., Bautz, M. W. & McNamara, B. R. Chandra imaging of the outer accretion flow onto the black hole at the center of the Perseus cluster. *Astrophys. J.* **850**, L3–L8 (2017).
69. Reis, R. C., Reynolds, M. T., Miller, J. M. & Walton, D. J. Reflection from the strong gravity regime in a lensed quasar at redshift $z = 0.658$. *Nature* **507**, 207–209 (2014).
70. Chartas, G. et al. Revealing the structure of an accretion disk through energy-dependent X-ray microlensing. *Astrophys. J.* **757**, 137–148 (2012).
71. Mosquera, A. M. et al. The structure of the X-ray and optical emitting regions of the lensed quasar Q 2237+0305. *Astrophys. J.* **769**, 53–60 (2013).
72. Blackburne, J. A., Kochanek, C. S., Chen, B., Dai, X. & Chartas, G. The optical, ultraviolet, and X-ray structure of the quasar HE 0435–1223. *Astrophys. J.* **789**, 125–135 (2014).
73. Tombesi, F., Cappi, M., Reeves, J. N. & Braito, V. Evidence for ultrafast outflows in radio-quiet AGNs—III. Location and energetics. *Mon. Not. R. Astron. Soc.* **422**, L1–L5 (2012).
74. Nardini, E. et al. Black hole feedback in the luminous quasar PDS 456. *Science* **347**, 860–863 (2015).
This paper presents strong evidence for feedback driven by the SMBH in a quasar.
75. Parker, M. L. et al. The response of relativistic outflowing gas to the inner accretion disk of a black hole. *Nature* **543**, 83–86 (2017).
76. Kara, E., Miller, J. M., Reynolds, C. & Dai, L. Relativistic reverberation in the accretion flow of a tidal disruption event. *Nature* **535**, 388–390 (2016).
Reverberation mapping of Fe K α in a TDE discovers accretion at 100 times the Eddington rate.
77. Miller, J. M. et al. Flows of X-ray gas reveal the disruption of a star by a massive black hole. *Nature* **526**, 542–545 (2015).
78. Lin, D. et al. A likely decade-long sustained tidal disruption event. *Nat. Astron.* **1**, 0033 (2017).
79. Lin, D. et al. A luminous X-ray outburst from an intermediate-mass black hole in an off-centre star cluster. *Nat. Astron.* **2**, 656–661 (2018).
80. Gierliński, M., Middleton, M., Ward, M. & Done, C. A periodicity of ~ 1 h in X-ray emission from the active galaxy RE J1034+396. *Nature* **455**, 369–371 (2008).
81. Reis, R. C. et al. A 200-second quasi-periodicity after the tidal disruption of a star by a dormant black hole. *Science* **337**, 949–951 (2012).
82. Pasham, D. J. et al. A loud quasi-periodic oscillation after a star is disrupted by a massive black hole. *Science* **363**, 531–534 (2019).

83. Miniutti, G. et al. Nine-hour X-ray quasi-periodic eruptions from a low-mass black hole galactic nucleus. *Nature* **573**, 381–384 (2019).
Discovery of powerful (100 times) eruptions from a low-mass nuclear BH with a 9-h period.
84. Brandt, W. N. & Alexander, D. M. Cosmic X-ray surveys of distant active galaxies. The demographics, physics, and ecology of growing supermassive black holes. *Astron. Astrophys. Rev.* **23**, 1–92 (2015).
85. Lapi, A. et al. The coevolution of supermassive black holes and massive galaxies at high redshift. *Astrophys. J.* **782**, 69–93 (2014).
86. Buchner, J. et al. Obscuration-dependent evolution of active galactic nuclei. *Astrophys. J.* **802**, 89–110 (2015).
87. Rangel, C. et al. Evidence for two modes of black hole accretion in massive galaxies at $z \sim 2$. *Mon. Not. R. Astron. Soc.* **440**, 3630–3644 (2014).
88. Georgakakis, A. et al. The X-ray luminosity function of active galactic nuclei in the redshift interval $z=3-5$. *Mon. Not. R. Astron. Soc.* **453**, 1946–1964 (2015).
89. Aird, J. et al. The evolution of the X-ray luminosity functions of unabsorbed and absorbed AGNs out to $z \sim 5$. *Mon. Not. R. Astron. Soc.* **451**, 1892–1927 (2015).
90. Nanni, R., Vignali, C., Gilli, R., Moretti, A. & Brandt, W. N. The X-ray properties of $z=6$ luminous quasars. *Astron. Astrophys.* **603A**, 128–139 (2017).
91. Pacucci, F., Ferrara, A., Volonteri, M. & Dubus, G. Shining in the dark: the spectral evolution of the first black holes. *Mon. Not. R. Astron. Soc.* **454**, 3771–3777 (2015).
92. Chilingarian, I. V. et al. A population of bona fide intermediate-mass black holes identified as low-luminosity active galactic nuclei. *Astrophys. J.* **863**, 1–15 (2018).
93. Mezcua, M., Civano, F., Fabbiano, G., Miyaji, T. & Marchesi, S. A population of intermediate-mass black holes in dwarf starburst galaxies up to redshift $z=1.5$. *Astrophys. J.* **817**, 20–29 (2016).
94. Baldassare, V. F., Reines, A. E., Gallo, E. & Greene, J. E. A $\sim 50,000 M_{\odot}$ solar mass black hole in the nucleus of RGG 118. *Astrophys. J.* **809**, L14–L19 (2015).
95. Pardo, K. et al. X-ray detected active galactic nuclei in dwarf galaxies at $0 < z < 1$. *Astrophys. J.* **831**, 203–217 (2016).
96. Komossa, S. et al. Discovery of a binary active galactic nucleus in the ultraluminous infrared galaxy NGC 6240 using Chandra. *Astrophys. J.* **582**, L15–L19 (2003).
97. Green, P. J. et al. SDSS J1254+0846: a binary quasar caught in the act of merging. *Astrophys. J.* **710**, 1578–1588 (2010).
98. Ellison, S. L., Secrest, N. J., Mendel, J. T., Satyapal, S. & Simard, L. Discovery of a dual active galactic nucleus with ~ 8 kpc separation. *Mon. Not. R. Astron. Soc.* **470**, L49–L53 (2017).
99. Koss, M. et al. Chandra discovery of a binary active galactic nucleus in Mrk 739. *Astrophys. J.* **735**, L42–L48 (2011).
100. Comerford, J. M., Pooley, D., Gerke, B. F. & Madejski, G. M. Chandra observations of a 1.9 kpc separation double X-ray source in a candidate dual active galactic nucleus galaxy at $z = 0.16$. *Astrophys. J.* **737**, L19–L23 (2011).
101. Gu, L. et al. Observations of a pre-merger shock in colliding clusters of galaxies. *Nat. Astron.* **3**, 838–843 (2019).
102. Fabian, A. C. Observational evidence of active galactic nuclei feedback. *Annu. Rev. Astron. Astrophys.* **50**, 455–489 (2012).
103. Forman, W. et al. Partitioning the outburst energy of a low Eddington accretion rate AGN at the center of an elliptical galaxy: the recent 12 Myr history of the supermassive black hole in M87. *Astrophys. J.* **844**, 122–143 (2017).
104. Arevalo, P., Churazov, E., Zhuravleva, I., Forman, W. R. & Jones, C. On the nature of X-ray surface brightness fluctuations in M87. *Astrophys. J.* **818**, 14–29 (2016).
105. Fabian, A. C. et al. A very deep Chandra observation of the Perseus cluster: shocks, ripples and conduction. *Mon. Not. R. Astron. Soc.* **366**, 417–428 (2006).
106. McNamara, B. R. & Nulsen, P. E. J. Mechanical feedback from active galactic nuclei in galaxies, groups and clusters. *New J. Phys.* **14**, 055023–055062 (2012).
107. Hardcastle, M. et al. Deep Chandra observations of Pictor A. *Mon. Not. R. Astron. Soc.* **455**, 3526–3545 (2016).
108. McDonald, M. et al. Deep Chandra, HST-COS, and MegaCam observations of the Phoenix cluster: extreme star formation and AGN feedback on hundred kiloparsec scales. *Astrophys. J.* **811**, 111–128 (2015).
109. Hlavacek-Larrondo, J. et al. X-ray cavities in a sample of 83 SPT-selected clusters of galaxies: tracing the evolution of AGN feedback in clusters of galaxies out to $z=1.2$. *Astrophys. J.* **805**, 35–47 (2015).
Demonstrates that AGN feedback in clusters of galaxies is a long-term (about 7 Gyr) phenomenon.
110. Giardini, S. et al. Radio galaxy feedback in X-ray-selected groups from COSMOS: the effect on the intracluster medium. *Astrophys. J.* **714**, 218–228 (2010).
111. Leauthaud, A. et al. A weak lensing study of X-ray groups in the Cosmos Survey: form and evolution of the mass–luminosity relation. *Astrophys. J.* **709**, 97–114 (2010).
112. Mantz, A. B. et al. The metallicity of the intracluster medium over cosmic time: further evidence for early enrichment. *Mon. Not. R. Astron. Soc.* **472**, 2877–2888 (2017).
113. Böhringer, H. & Werner, N. X-ray spectroscopy of galaxy clusters: studying astrophysical processes in the largest celestial laboratories. *Astron. Astrophys. Rev.* **18**, 127–196 (2010).
114. de Plaa, J. et al. CHEERS: the chemical evolution RGS sample. *Astron. Astrophys.* **607**, 98–113 (2017).
115. Mernier, F. et al. Radial metal abundance profiles in the intra-cluster medium of cool-core galaxy clusters, groups, and ellipticals. *Astron. Astrophys.* **603**, 80–106 (2017).
116. Wang, T. et al. Discovery of a galaxy cluster with a violently starbursting core at $z=2.506$. *Astrophys. J.* **828**, 56–70 (2016).
117. Su, Y. et al. Deep Chandra observations of NGC 1404: cluster plasma physics revealed by an infalling early-type galaxy. *Astrophys. J.* **834**, 74–82 (2017).
118. Eckert, D. et al. Deep Chandra observations of the stripped galaxy group falling into Abell 2142. *Astron. Astrophys.* **605**, A25–A36 (2017).
119. Sanders, J. et al. A very deep Chandra view of metals, sloshing and feedback in the Centaurus cluster of galaxies. *Mon. Not. R. Astron. Soc.* **457**, 82–109 (2016).
120. Walker, S. A., Zuhone, J., Fabian, A. & Sanders, J. The split in the ancient cold front in the Perseus cluster. *Nat. Astron.* **2**, 292–296 (2018).
121. Cen, R. & Ostriker, J. P. Where are the baryons? *Astrophys. J.* **514**, 1–6 (1999).
122. Eckert, D. et al. Warm-hot baryons comprise 5–10 per cent of filaments in the cosmic web. *Nature* **528**, 105–107 (2015).
123. Nicastro, F. et al. Observations of the missing baryons in the warm-hot intergalactic medium. *Nature* **558**, 406–409 (2018).
These two papers (refs. 123 and 124) report significant detection of the WHIM, thought to be the location of the missing baryons.
124. Kovacs, O. E., Bogdan, A., Smith, R. K., Kraft, R. P. & Forman, W. R. Detection of the missing baryons toward the sightline of H1821+643. *Astrophys. J.* **872**, 83K (2019).
125. Gaggero, D. et al. Searching for primordial black holes in the radio and X-ray sky. *Phys. Rev. Lett.* **118**, 241101 (2017).
126. Harvey, D., Massey, R., Kitching, T., Taylor, A. & Tittley, E. The non-gravitational interactions of dark matter in colliding galaxy clusters. *Science* **347**, 1462–1465 (2015).
This study places constraints on the self-interaction cross-section of dark matter based on multiwavelength observations of interacting clusters of galaxies.
127. Kravtsov, A. V. & Borgani, S. Formation of galaxy clusters. *Annu. Rev. Astron. Astrophys.* **50**, 353–409 (2012).
128. Mantz, A. B. et al. Cosmology and astrophysics from relaxed galaxy clusters—II. Cosmological constraints. *Mon. Not. R. Astron. Soc.* **440**, 2077–2098 (2014).
129. Mantz, A. B. et al. Weighing the giants—IV. Cosmology and neutrino mass. *Mon. Not. R. Astron. Soc.* **446**, 2205–2225 (2015).
130. Pierre, M. et al. The XXL Survey. I. Scientific motivations—XMM-Newton observing plan - Follow-up observations and simulation programme. *Astron. Astrophys.* **592**, 1–15 (2016).
131. Pacaud, F. et al. The XXL Survey. II. The bright cluster sample: catalogue and luminosity function. *Astron. Astrophys.* **592**, A2–A26 (2016).
132. Planck Collaboration. Planck 2015 results. XXIV. Cosmology from Sunyaev-Zeldovich cluster counts. *Astron. Astrophys.* **594**, A24–A42 (2016).
133. Risaliti, G. & Lusso, E. A Hubble diagram for quasars. *Astrophys. J.* **815**, 33–48 (2015).
134. Risaliti, G. & Lusso, E. Cosmological constraints from the Hubble diagram of quasars at high redshift. *Nat. Astron.* **3**, 272–277 (2019).
This study develops a tool for measuring cosmological distances at high redshift using the optical versus ultraviolet luminosity in quasars; the results suggest a deviation at high redshifts.
135. Medvedev, P., Gilfanov, M., Sazonov, S., Scharrel, N. & Sunyaev, R. XMM-Newton observations of the extremely X-ray luminous quasar CFHQS J142952+544716 at redshift $z = 6.18$. *Mon. Not. R. Astron. Soc.* **504**, 576–582 (2021).
136. Barcons, X. et al. Athena: ESA's X-ray observatory for the late 2020s. *Astron. J.* **338**, 153–158 (2017).
137. Lynx Team The Lynx Mission Concept Study Interim Report. Preprint at <https://arxiv.org/abs/1809.09642> (2018).
138. Wilkes, B. & Tucker, W. (eds) *The Chandra X-ray Observatory Exploring the High Energy Universe* (IOP, 2019).
A comprehensive review of Chandra and its place within astronomy and its science authored by experts in their respective fields.
139. Schwartz, D. A. et al. Chandra discovery of a 100 kiloparsec X-ray jet in PKS 0637-752. *Astrophys. J.* **540**, 69–72 (2000).
140. Tamura, T. et al. X-ray spectroscopy of the cluster of galaxies Abell 1795 with XMM-Newton. *Astron. Astrophys.* **365**, L87–L92 (2001).
141. Fabian, A. C. et al. A deep Chandra observation of the Perseus cluster: shocks and ripples. *Mon. Not. R. Astron. Soc.* **344**, L43–L47 (2003).
142. Igoshev, A. P., Hollerbach, R., Wood, T. & Gourgoulatis, K. N. Strong toroidal magnetic fields required by quiescent X-ray emission of magnetars. *Nat. Astron.* **5**, 145–149 (2021).
143. Alston, W. N. A. et al. A dynamic black hole corona in an active galaxy through X-ray reverberation mapping. *Nat. Astron.* **4**, 597–602 (2020).
Measurements of both spin and mass for a BH with reverberation mapping.

Acknowledgements It is an honour, privilege and pleasure to serve on the teams responsible for Chandra and XMM-Newton, and to acknowledge their dedication and excellence over so many years. We acknowledge and thank both NASA and ESA for their continued support for these two missions. We acknowledge the contributions of thousands of individuals, both within the mission projects and around the world, who have worked hard to make these observatories successful. B.J.W. and W.T. acknowledge support from NASA contract NAS8-03060 (Chandra X-ray Center). B.J.W. acknowledges support from the Royal Society and the Wolfson Foundation while at the University of Bristol, UK, and thanks the Institute of Astronomy, Cambridge University, UK, for their hospitality, and the support of a Sheepshank Visiting Fellowship during part of this work.

Author contributions In keeping with the synergistic nature of the Chandra and XMM-Newton missions, all the sections of the manuscript contained discussions of the scientific discoveries made by both Chandra and XMM-Newton. B.J.W. and W.T. concentrated on results from Chandra, and N.S. and M.S.-L. focused on XMM-Newton.

Competing interests The authors declare no competing interests

Additional information

Correspondence and requests for materials should be addressed to Belinda J. Wilkes.

Peer review information Nature thanks Richard Mushotzky and Christopher Reynolds for their contribution to the peer review of this work.

Reprints and permissions information is available at <http://www.nature.com/reprints>.

Publisher's note Springer Nature remains neutral with regard to jurisdictional claims in published maps and institutional affiliations.